PNAS

www.pnas.org

Supplementary Information for

The multi-faceted mechano-bactericidal mechanism of nanostructured surfaces

Elena P. Ivanova[a,b], Denver P. Linklater[a], Marco Werner [c], Vladimir A. Baulin[d], XiuMei Xu[e], Nandi Vrancken[e, f], Sergey Rubanov[g], Eric Hanssen[g,h], Jason Wandiyanto[i], Vi Khanh Truong[a], Aaron Elbourne[a], Shane Maclaughlin[b], Saulius Juodkazis[i], Russell J. Crawford[a]

Correspondence: Elena P. Ivanova
Email: elena.ivanova@rmit.edu.au

This PDF file includes:

> Supplementary text: experimental methods and discussion
> Figures S1 to S6
> Tables S1
> Supplementary References

1

Supplementary Methods

Contact angle measurements. Static water contact angles were measured on the substratum surfaces using the sessile drop method as described previously.(1, 2) The wettability of these surfaces are previously determined and described elsewhere.(3) The contact angle measurements were carried out in air using an FTA1000c instrument equipped with a nano-dispenser (First Ten Ångstroms, Inc., Portsmouth, VA, U.S.A.). The volume of the droplets used for analysis was approximately 1.0 µL. The contact angles were measured by recording 50 images over 2 s with a Pelcomodel PCHM 575-4 camera and measuring the contact angles after the droplet had been rested on the surface for approximately one second.

Surface Chemical Characterisation (XPS). XPS analysis was performed using a Thermo ScientificTM K-alpha X-ray Photoelectron Spectrometer (ThermoFischer), equipped with a monochromatic X-ray source (Al Kα, hv = 1486.6 eV) operating at 150 W. The spectrometer energy scale was calibrated using the Au 4f7/2 photoelectron peak at the binding energy (BE) of 83.98 eV. During analysis, the samples were flooded with low-energy electrons to counteract any surface charging that may take place. The hydrocarbon component of the C 1s peak (binding energy 284.8 eV) was used as a reference for charge correction. Photoelectrons emitted at 90° to the surface from an area of 700×300 µm^2 were analysed with 160 eV for survey spectra and then with 20 eV for region spectra. Survey spectra were recorded at 1.0 eV/step, while the region spectra were taken at 0.1 eV/step. The Shirley algorithm was used to measure the background core level spectra and chemically distinct species in the high-resolution regions of the spectra were resolved using synthetic Gaussian–Lorentzian components after the background was removed (using the Thermo ScientificTM Avantage Data System). The relative atomic concentration of elements determined using XPS was quantified based on the peak area in the selected high-resolution region, with the appropriate sensitivity factors for the instrument being used. High resolution scans were performed across each of the carbon 1s, oxygen 1s, fluorine 1s, nitrogen 1s and silicon 2p $^{3/2}$ and $^{1/2}$ peaks.

AFM characterisation. Images were obtained using a combination of MFP-3D and Cypher ES Atomic Force Microscopes (Oxford Instrument, Asylum Research, Santa Barbara, CA, USA) at room temperature (25°C)using amplitude modulated-AFM (AM-AFM). Image reproducibility was confirmed by using two separate cantilevers: either an OMCL-AC240TS (Olympus Corporation, Japan, nominal spring constant kc= 2 N/m) or Arrow UHF (NanoWorld, Switzerland, nominal spring constant kc= 6 N/m). The cantilevers employed in this study are commercially available and exhibit a sharp, reduced tip radius over the entirety of their profile. To minimise the imaging force, a set-point ratio (Imaging Amplitude (A)/free amplitude (A0)) of >0.7–0.8 was maintained during imaging (unless otherwise stated). Cantilevers were calibrated using the thermal spectrum method, in liquid prior to use, and the lever sensitivity was deter-mined using force spectroscopy; the spring constant is resolved via the inverse optical lever sensitivity (In VOLS) using force curve measurements on the hard surface. Force spectroscopic analysis revealed no finer interfacial details. The features of all images presented here rotated as the scan angle was changed and scaled correctly with scan size. This approach confirmed that the images were not a result of scanning artefacts. During image acquisition both the trace (scanning left to right) and retrace (scanning right to left) profiles were superimposed, meaning that a true representation of the surface was obtained. Using this protocol, tip-based convolution effects are significantly minimised.

Attachment propensity on the nanopillared surfaces. Analysis of the CLSM images and quantification of cellular attachment (Fig. 4) showed that the attachment density gradually decreased as the nanopillar height on the substratum was increased. The substratum with 220 nm pillars exhibited the largest number of attached bacteria of both species while, in comparison, on substrata possessing 360 and 420 nm pillars, the average attachment rates of *P. aeruginosa* and *S. aureus* cells decreased by ~30%, and ~40%, respectively. The decreased extent of bacterial attachment, which corresponds to increasing nanopillar height appears to be independent bacterial species studied, *i.e.,* the cells of two bacterial species differ greatly in their size, morphology, membrane rigidity and motility.(4)

Supplementary Discussion

Bacterial interactions with surfaces in liquid conditions

In liquid conditions, bacterial motility is influenced by Brownian motion. In particular, the random movement of bacteria is governed by their collisions with surrounding water molecules in thermodynamic equilibrium.(5) When the Reynolds number is very low, meaning that inertial effects are negligible, bacteria cannot 'coast' in liquid but must constantly input energy in order to swim. For motile bacteria that rely on a single polar flagellum for propulsion, such as *Pseudomonas aeruginosa* used in this study, Brownian motion enables them to change direction, increasing their ability to find nutrients. Several studies have investigated the near-surface swimming of bacteria. It was reported that motile bacteria 'slow down' on approach to a solid surface and turn to swim parallel close to the surface for some time. A sphere with the same physical proportions would have diffused away from the surface almost immediately due to Brownian motion. However, hydrodynamic interactions can keep the cell closer to the surface for longer periods.(6) These long stable trajectories in close proximity to a surface can eventually promote cellular attachment.(7)

Impact of material stiffness on cell adhesion and survival

While very little work has been done to elucidate the role of pillar elasticity on bacterial adhesion and behavior on nanostructured surfaces, interestingly, the stiffness of flat materials has been found to influence the bacterial adhesion to a surface. In one study, material stiffness of polyelectrolyte multilayer (PEM) thin films was found to impact bacterial adhesion to a greater degree than other physicochemical properties of the surface such as surface roughness, interaction energy, and charge density. Bacteria preferentially adhered to materials with a higher stiffness.(8) The bacterial adhesion to a flat, elastic surface was also investigated using poly(dimethylsiloxane) (PDMS) surfaces exhibiting different stiffness based on varying concentrations of plasticizer.(9, 10) The results indicated that, in addition to sensing the general contact with a surface, bacteria have specific genes involved in response to material stiffness during attachment. Material stiffness may, in fact, determine biofilm formation by manipulating attachment and cell motility. In contrast to the above work, motile *E. coli* cells preferred to adhere to less stiff PDMS surfaces. When considering the impact of smooth material stiffness on eukaryotic cell adhesion and cell spreading, an increase in the material stiffness has been shown to lead to higher efficiency of phagocytosis of attached *E. coli* cells.(9) This is because macrophages exhibit higher motility while bacterial cells maintain a smaller size when attached to stiff surfaces compared to elastic ones. Collectively, the results indicated that material stiffness is an important factor that affects the interaction between bacteria and host cells.

In contrast to smooth surfaces, the influence of pillar elasticity on eukaryotic cell adhesion and behavior, has been studied in depth. Micropillar arrays have been used extensively to study cell spreading and migratory behavior. Cells can sense the substratum using cytoskeletal contractions, which are assumed to be absent in bacteria, and can cause the deflection of micropillar arrays by traction forces generated by actin re-arrangement. Evaluation of pillar deflections can inform
One study reported the deflection of sub-micron pillar arrays just by membrane adhesion, before mature adhesion and stress fibers were formed.(11) On elastomeric micropillar arrays with gradient stiffness, eukaryotic cells were found to preferentially attach to pillar arrays with a greater stiffness and exhibited a pronounced elongated morphology in the direction parallel to the pillar arrays.(12, 13) This occurs because the cell should minimize the energy they must invest for attachment to the elastic anisotropic medium by preferentially spreading along the direction of maximal stiffness.(14)

Despite the possibility of piconewton resolution in force measurements based on the deflection of nanopillar arrays, this methodology has not been extended to routinely study the adhesion of prokaryotic cells to surfaces. In contrast to eukaryotic cells, bacteria in suspension behave more like colloidal particles (as described above). Therefore, the responses of bacteria and mammalian cells during attachment to nano-microstructured surfaces are very different. Unlike eukaryotic cells,

microbial cells are quite rigid, with a Young's modulus (E) of live *E. coli* cells being 1.9 ± 0.9 to 3.0 ± 0.6 MPa, and 6.1 ±1.5 MPa for dead *E. coli*.(15) As such, they have well-defined shapes that do not deform easily and are unlikely to generate high enough traction forces to deflect micropillars with dimensions of 1–3 µm in diameter, and relative spacing. Nevertheless, when considering *nanopillar* arrays, the role of pillar stiffness influencing the attachment and behavior of bacterial cells can also be studied. During bacteria-surface attachment, bacteria respond to the surface (mechano-sensing) through changes in tension of the cell membrane generating a mechanical stress yielding membrane deformation. InP nanowires have been investigated to sense the corresponding forces involved during bacterial attachment to a nanopatterned surface possessing elastic pillar arrays. Membrane adhesion, and even thin filaments such as flagella, could exert sufficient force to deflect the nanopillars (in the range of 20-70 nN).(16)

Supplementary Results

Euler–Bernoulli theory of bending

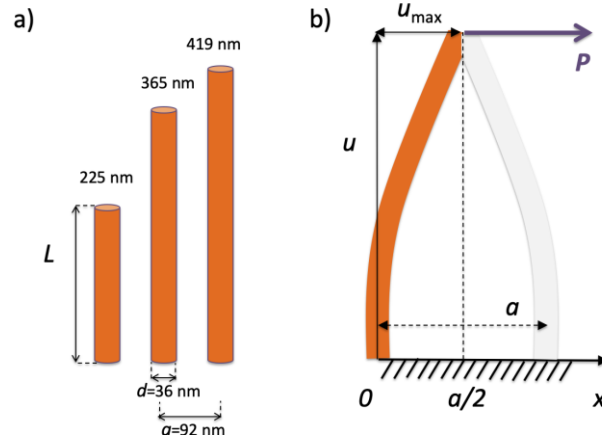Consider two pillars clustered together, as depicted in Figure S1.

Figure S1. **Nanopillars dimensions and scale**. (a) Diameter d = 36 nm, the distance between pillars a = 92 nm. The samples differ only with the length L=225 nm, 365 nm, 419 nm (true aspect ratio). (b) Schematic illustration of pillar bending for calculation of the bending elasticity and strain energy stored in pillars.

This configuration is characterized by the balance between molecular attraction forces acting between the two tips of the pillars, external force P (load), and the elastic force of the pillars. Due to symmetry, two pillars tips meet, on average, at a half distance between the pillars, $a/2$. Thus, molecular forces acting at the tip of a pillar will be equal to the load, P, inducing maximum deflection of the tip of a single pillar, u_{max}, to the distance $a/2$ and, therefore, can be calculated. The deflection $u(x)$ of a pillar due to momentum, M, applied at the tip of the pillar as a function of a distance x is given by

$$\frac{d^2 u(x)}{dx^2} = \frac{M}{EI} \qquad\qquad \text{(S1)}$$

This gives the profile of a bent pillar as a distance x. The deflection of a tip is given by the maximum displacement u_{max}, induced by the force, P, acting on the tip $u_{max} = \frac{PL^3}{3EI}$, or in dimensionless form

$$\frac{u_{max}}{a} = \frac{1}{3}\left[\frac{Pa^2}{EI}\right](L/a)^3 \qquad\qquad \text{(S2)}$$

where E is the elastic modulus, and I is the area moment of inertia, which depends on the cross-section shape of the pillar. For the given shape of the pillars, EI, also known as flexural rigidity, is a constant and can be calculated.

The dimensionless parameter, reduced force $\beta = \frac{Pa^2}{EI}$ controls the strength of pillar attraction with respect to pillar bending rigidity. The maximum deflection for different β is shown in Figure 2. Pillars can touch each other when the maximum deflection due to external forces, such as the attachment of a bacterial cell, is more significant than the interpillar half-distance $a/2$. Thus, according to these estimates, longer pillars, L=420 nm, require two orders of magnitude less of externally applied force to be able to interact between each other than shorter pillars, L=225 nm.

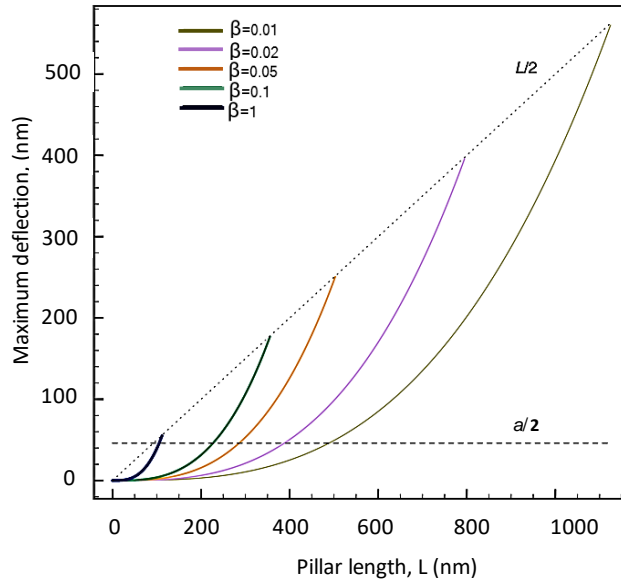**Figure S2.** Maximum tip deflection u_{max} as a function of pillar height L for different values of effectively reduced force acting between pillars β for interpillar distance $a = 92$ nm. The dashed line corresponds to half-distance between pillars $a/2$. The dotted line is a half-length of the pillars $L/2$.
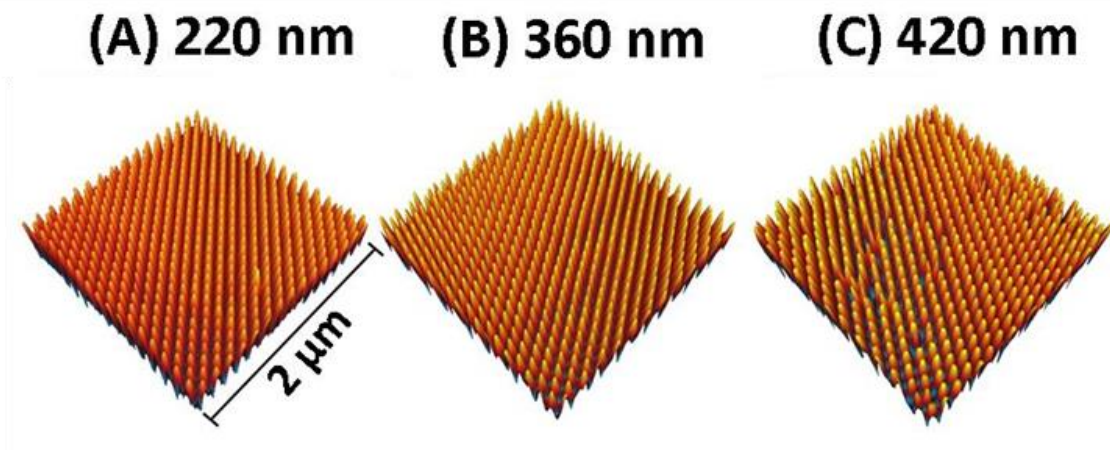
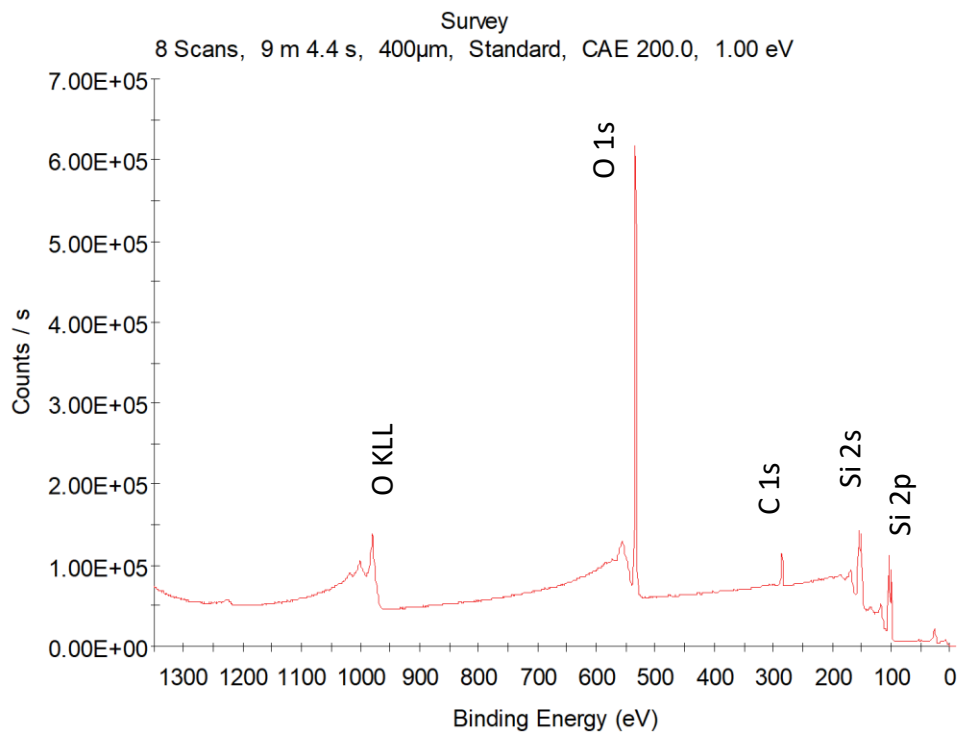**Fig. S3.** 2 μm × 2 μm AM-AFM images rendered in 3D of the respective surfaces imaged in air.

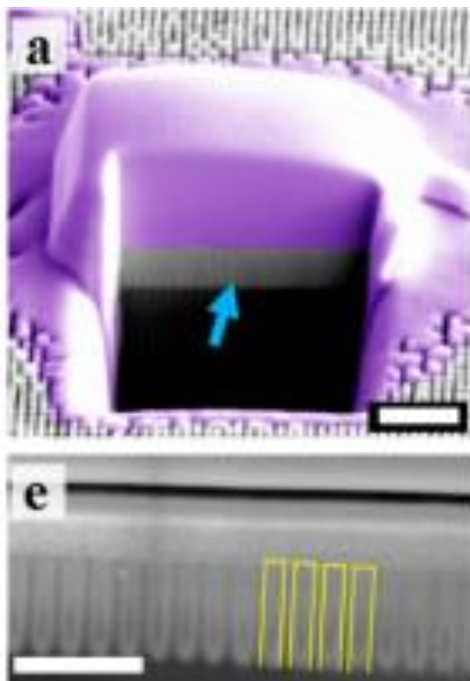**Fig. S4.** XPS survey spectra of nanopillared Si surfaces.

Fig. S5. A representative focused ion beam – scanning electron microscopy (FIB-SEM) image of the bacterial-nanopillar interface following Pt deposition. The Pt passivation layer has been false-coloured purple, and the blue arrow indicates the cross-section of samples exposed following ion-beam milling. E) A close-up of the exposed surface side-profile (blue arrow), and the surrounding uncoated nanopillars is also shown.
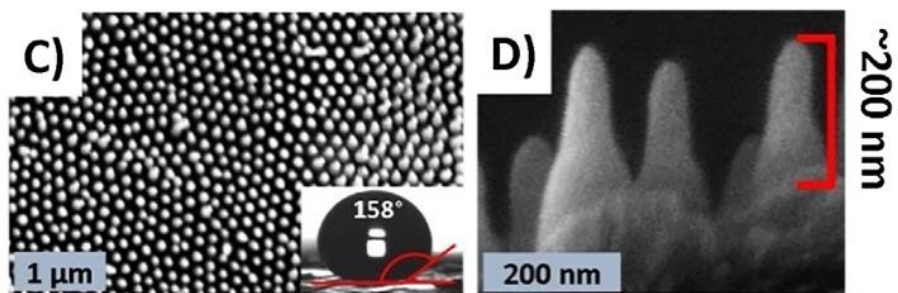
Nanopillars
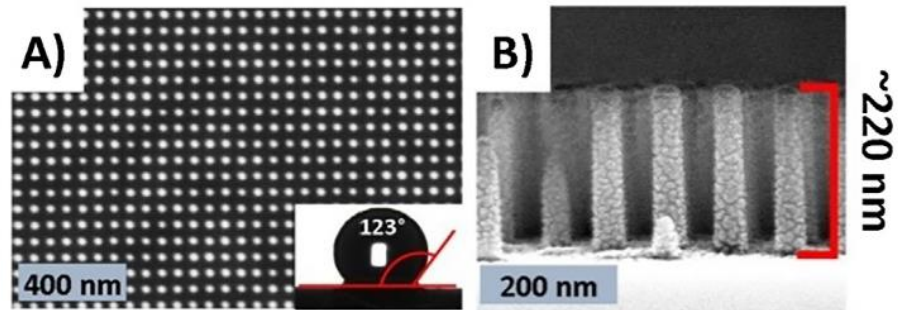
Cicada Wing

Fig. S6. A comparison of the surface geometry of as-fabricated Si surfaces and native cicada wing surfaces. Although a semi-regular pattern, Cicada wing surfaces are only able to effectively inactivate Gram-negative bacteria. Adapted with permission from Elbourne*, et al.* (3).

Table S1. Topographical parameters and physico-chemical properties of silicon nanopillar arrays

Sample	220 nm	360 nm	420 nm	Flat Si
Topographical Parameters				
Nanopillar height (L) (nm)[a]	224.7 ± 4.3	364.7 ± 2.4	419.4 ± 4.2	-
Aspect ratio	6	10	12	-
Surface roughness (R_a)(nm)	2.31	3.01	4.08	-
Wettabilty (water contact angle °)				
	122.3 ± 3.7	126.7 ± 0.9	140.6 ± 6.8	51.8 ± 0.5
Surface Chemical Characterisation (Atomic %)				
F1s	0.44	0.87	0.76	-
Si2p	38.39	39.55	39.19	58.65
N1s	0.48	0.2	0.25	0.39
C1s	10.81	10.29	10.2	9.98
O1s	44.98	44.38	44.98	30.98
S2p	4.9	4.71	4.62	-

References

1. Bhadra CM*, et al.* (2015) Antibacterial Titanium Nano-patterned Arrays Inspired by Dragonfly Wings. *Sci. Rep.* 5:16817.
2. Ivanova EP*, et al.* (2013) Bactericidal Activity of Black Silicon. *Nat. Commun.* 4:2838.
3. Elbourne A*, et al.* (2019) Imaging the air-water interface: Characterising biomimetic and natural hydrophobic surfaces using in situ atomic force microscopy. *Journal of Colloid and Interface Science* 536:363-371.
4. Harvey RA (2007) *Microbiology* (Lippincott Williams & Wilkins).
5. Li G, Tam LK, & Tang JX (2008) Amplified effect of Brownian motion in bacterial near-surface swimming. *Proceedings of the National Academy of Sciences* 105(47):18355-18359.
6. Frymier PD, Ford RM, Berg HC, & Cummings PT (1995) Three-dimensional tracking of motile bacteria near a solid planar surface. *Proceedings of the National Academy of Sciences* 92(13):6195-6199.
7. Giacché D, Ishikawa T, & Yamaguchi T (2010) Hydrodynamic entrapment of bacteria swimming near a solid surface. *Physical Review E* 82(5).
8. Lichter JA*, et al.* (2008) Substrata Mechanical Stiffness Can Regulate Adhesion of Viable Bacteria. *Biomacromolecules* 9(6):1571-1578.
9. Zhao Y, Song F, Wang H, Zhou J, & Ren D (2017) Phagocytosis of Escherichia coli biofilm cells with different aspect ratios: a role of substratum material stiffness. *Applied Microbiology and Biotechnology* 101(16):6473-6481.
10. Song F*, et al.* (2017) How Bacteria Respond to Material Stiffness during Attachment: A Role of Escherichia coli Flagellar Motility. *ACS Applied Materials & Interfaces* 9(27):22176-22184.
11. Ghassemi S*, et al.* (2012) Cells test substrate rigidity by local contractions on submicrometer pillars. *Proceedings of the National Academy of Sciences* 109(14):5328-5333.
12. Wang B, Shi J, Wei J, Tu X, & Chen Y (2019) Fabrication of elastomer pillar arrays with elasticity gradient for cell migration, elongation and patterning. *Biofabrication* 11(4):045003.
13. Wei J*, et al.* (2016) Fabrication of adjacent micropillar arrays with different heights for cell studies. *Microelectronic Engineering* 158:22-25.
14. Saez A, Ghibaudo M, Buguin A, Silberzan P, & Ladoux B (2007) Rigidity-driven growth and migration of epithelial cells on microstructured anisotropic substrates. *Proceedings of the National Academy of Sciences* 104(20):8281-8286.
15. Cerf A, Cau J-C, Vieu C, & Dague E (2009) Nanomechanical Properties of Dead or Alive Single-Patterned Bacteria. *Langmuir* 25(10):5731-5736.
16. Sahoo PK*, et al.* (2016) Nanowire Arrays as Cell Force Sensors To Investigate Adhesin-Enhanced Holdfast of Single Cell Bacteria and Biofilm Stability. *Nano Letters* 16(7):4656-4664.